



High accuracy neural network interatomic potential for NiTi shape memory alloy

Hao Tang^a, Yin Zhang^b, Qing-Jie Li^b, Haowei Xu^b, Yuchi Wang^c, Yunzhi Wang^c, Ju Li^{a,b,*}

^a Department of Materials Science and Engineering, Massachusetts Institute of Technology, MA 02139, USA

^b Department of Nuclear Science and Engineering, Massachusetts Institute of Technology, MA 02139, USA

^c Department of Materials Science and Engineering, The Ohio State University, 2041 College Road, Columbus, OH 43210, USA



ARTICLE INFO

Article history:

Received 28 February 2022

Revised 15 July 2022

Accepted 28 July 2022

Available online 30 July 2022

ABSTRACT

Nickel-titanium (NiTi) shape memory alloys (SMA) are widely used, however simulating the martensitic transformation of NiTi from first principles remains challenging. In this work, we developed a neural network interatomic potential (NNIP) for near-equiatomic Ni-Ti system through active-learning based acquisitions of density functional theory (DFT) training data, which achieves state-of-the-art accuracy. Phonon dispersion and potential-of-mean-force calculations of the temperature-dependent free energy have been carried out. This NNIP predicts temperature-induced, stress-induced, and defect-induced martensitic transformations from atomic simulations, in significant agreement with experiments. The NNIP can directly simulate the superelasticity of NiTi nanowires, providing a tool to guide their design.

© 2022 Published by Elsevier Ltd on behalf of Acta Materialia Inc.

1. Introduction

Shape memory alloys (SMA) are widely used in aerospace, automotive, and medical applications because of their temperature induced shape memory and stress-induced superelasticity/pseudoelasticity behavior [1,2]. The unique properties of SMA arise from its diffusionless martensitic transformation that provides inelastic strain without triggering ordinary dislocation plasticity (ODP). At zero stress, there are two well-known phases: the high-temperature stabilized austenite phase, and the low-temperature stabilized martensite phase. When there is stress, transforming to a particular orientational variant of the martensite phase can be preferred. The temperature-induced martensitic transformation leads to shape memory effects (SME), where arbitrary low-temperature inelastic strain distribution can ideally be wiped clean by increasing the temperature and driving back to the high-symmetry austenite phase. The stress-induced martensitic transformation (SIMT) also leads to superelastic behaviors, where the alloy deforms reversibly at the austenite-stabilizing temperature to high strain [3,4]. As the first SMA utilized in engineering application, the nearly equiatomic Ni-Ti system have attracted extensive research interests due to its good mechanical properties and martensitic transformation temperature close to the room temperature [4–6]. The martensitic transformation of NiTi is from the

cubic B2 phase (high temperature stable) to the monoclinic B19' phase (low temperature stable), whose small free energy difference is switched at the transformation temperature. Depending on the composition, Ni-Ti can displays complex microstructural evolution and properties with various metastable phases and deformation mechanisms [7–9]. Its martensitic transformation can be regulated by the concentration gradient [8,10,11], deformation twinning [12–15], and nanostructure [16–18], providing large engineering freedom for SMA design [2]. Extensive research has also focused on the atomistic simulation of NiTi martensitic transformation to better understand the underlying mechanism and accelerate alloy design [19–23].

However, simulating the phase transformation in NiTi remains challenging. As the energy difference of relevant phases in NiTi is very small [7], on the order of a few meV/atom, an accurate description of the free-energy profile, which depends sensitively on vibrational contributions, is necessary to capture the subtle temperature effect on phase stability. The density functional theory (DFT) calculations can provide an accurate description of the potential energy surface but are limited by its high computational cost [24]. Simulating the martensitic transformation-related phenomena usually requires a large supercell, making it difficult to use the DFT level ab initio molecular dynamics (AIMD) [24]. Previously, empirical interatomic potentials for NiTi system are developed by several methods, including embedded-atom method (EAM) [25–28], modified EAM (MEAM) [29–32], and 2nd nearest-neighbor (2NN) MEAM [33,34]. However, these methods cannot simultaneously describe all phases with high accuracy. Only the 2NN

* Corresponding author.

E-mail address: ljli@mit.edu (J. Li).

MEAM can qualitatively reproduce the general behavior of martensitic transformation, while its accuracy still has significant room to improve [33,34]. Alternatively, the recent development of neural network interatomic potential (NNIP) provides a way to balance the accuracy and computational cost [35,36]. Benefiting from the high expressivity of deep neural network, the accuracy and generalization ability of the NNIP can be successively improved through the active learning scheme [37] towards the DFT accuracy.

In this work, we developed an NNIP for near equiatomic NiTi trained on a comprehensive DFT dataset for the first time. This empirical potential exhibits state-of-the-art overall accuracy on atomic structure, energy, and elastic modulus for different phases of NiTi. The molecular dynamics (MD) simulation produces the temperature-induced martensitic transformation consistent with experiments. We then study the microstructure of twin boundaries, where the experimentally observed extended core structure is derived in the simulation. Finally, the superelasticity in NiTi nanowire is directly simulated by the NNIP, confirming its validity for nanostructures. The NNIP and DFT database are publicly available at a publicly accessible website (URL: <https://www.ctcms.nist.gov/potentials> Website DOI:10.18434/m37), providing an accurate theoretical tool for SMA simulation.

2. Methods

To implement the supervised learning scheme for the NNIP, a DFT database is firstly constructed with various configurations of Ni-Ti. The DFT calculations are implemented through the Vienna ab-initio simulation package (VASP) using the projector-augmented wave (PAW) method [38,39] with cut-off energy of 400 eV, and the 3p semi-core state of both Ni and Ti treated as valence states. The Perdew-Burke-Ernzerhof (PBE) functional of generalized gradient approximation (GGA) is used for electron exchange-correlation [40]. The k point mesh is set with a separation of 0.04 \AA^{-1} , and electronic iteration converges to 10^{-5} eV.

The neural network framework is constructed through DeepMD-kit [36]. The atomic configurations are firstly parametrized by the descriptor matrix that naturally preserves permutation and rotation symmetry [35]:

$$D_{ij}^\alpha = \left\{ \frac{1}{R_{ij}}, \frac{x_{ij}}{R_{ij}}, \frac{y_{ij}}{R_{ij}}, \frac{z_{ij}}{R_{ij}} \right\} \quad (1)$$

where R_{ij} and x_{ij}, y_{ij}, z_{ij} are the distance and relative coordinates between atom i and its neighbor atom j (α goes from 1 to 4 of the list). The atomic environment of each atom i is then represented by the $n \times 4$ matrix $[D_i]_{j\alpha}$, where j goes through all atoms within the cut-off radius (set to be 6 \AA) of interatomic interactions. We set n larger than the maximal possible number of atoms within the cut-off radius and fill zeros in the redundant rows. The descriptors are then forwarded to a multilayer perceptron (MLP) with three hidden layer to output the total energy:

$$E = \sum_i E_{s(i)} = \sum_i \mathcal{L}_{s(i)}^{\text{out}} \circ \mathcal{L}_{s(i)}^2 \circ \mathcal{L}_{s(i)}^1(\mathbf{D}_i) \quad (2)$$

where each mapping $\mathcal{L}_{s(i)}$ contains 480 neurons with hyperbolic tangent activation function. The loss function consists of the deviation of both energy and force

$$L \equiv \frac{p_e}{N} \Delta E^2 + \frac{p_f}{3N} \sum_i |\Delta F_i|^2 \quad (3)$$

where N , ΔE , and ΔF_i are the number of atoms, standard deviation of energy, and standard deviation of force on atom i . The weight coefficients are set linearly dependent on the training step t (t goes from 0 to 100,000) to get better convergence, where the initial and final values are: $p_e(t=0) = 0.01 \text{ eV}^{-2}$, $p_e(t=50000) = 1 \text{ eV}^{-2}$,

$p_f(t=0) = 1000 \text{ (eV/\AA)}^{-2}$, $p_f(t=100000) = 1 \text{ (eV/\AA)}^{-2}$. Details of the neural network algorithm are described in Ref. [35].

The sampling of DFT calculations begins from the equilibrium structure of bulk B2, B19', B19, B33, and R phases [7], and slab with (100) and (110) surfaces of the B2 phase (1000 data points for each, sampled by AIMD with $2 \times 2 \times 3$ supercell). Structures with slight off-stoichiometric compositions are included with one substitutional defect Ni_{Ti} or Ti_{Ni} in the supercell (1000 data points for each). Then, the active learning scheme is employed to include structures strongly deviate from equilibrium position (1000 data points), with supercell under strain (1000 data points), and stacking faults (1000 data points) [37]. Four models are trained simultaneously, and new structures where the models' predictions show the largest deviation are included in the DFT database for reinforcement training. The training database eventually includes 12,000 configurations where each configuration contains 48 atoms. The predicted energy and force are tested by randomly selected ten percents of configurations, and the standard validation error converges to $\Delta E = 4.1 \text{ meV/atom}$ and $|\Delta F| = 0.11 \text{ eV/\AA}$, respectively.

Molecular dynamics simulation through the NNIP is carried out by Large-scale Atomic/Molecular Massively Parallel Simulator (LAMMPS) [46] with Nosé-Hoover style thermal statistics [47]. The temperature-dependent free energy difference between B2 and B19' phases are computed through the potential-of-mean-force thermodynamic integration [48,49]:

$$F(\lambda_2, T) - F(\lambda_1, T) = \int_{\lambda_1}^{\lambda_2} \left\langle \frac{\partial \mathcal{H}}{\partial \lambda} \right\rangle_{\lambda=\lambda'} d\lambda' \quad (4)$$

where λ is the reaction coordinate that connects the B2 phase ($\lambda_1 = 0$) and B19' phase ($\lambda_2 = 1$), and the average of the partial derivative is calculated through temporal average of the MD trajectory at each different λ . Here λ denotes the cell shape (strain), and the generalized force is therefore just the stress.

3. Results

The accuracy of the NNIP on the five phases is examined by geometric, energetic, and strain response coefficients at zero temperature, as shown in Table 1. The NNIP shows better overall accuracy than the 2NN MEAM and Finnis-Sinclair model, consistently matching the DFT and experimental lattice parameters within 2%. Specifically, the atomic configuration of B19' phase by the 2NN-MEAM potential in Ref. [34] shows evident deviation from the DFT results, while the NNIP results show consistent agreement. The accuracy of the NNIP for bulk modulus is consistently within 10% for B2, B19', B19, and B33 phases, where the previous potentials sometimes give errors of about 20%. The previous potentials show significant error in the energy difference of phases (up to 60%), which is critical for the phase transformation behavior. In comparison, NNIP derives energy differences consistent with the DFT within 10%. The lattice parameters and energy of the R phase from the NNIP is also well consistent with the DFT, which has not been tested for other empirical potentials. The bulk modulus of the R-phase NiTi from the NNIP is 14% larger than that from the DFT results. We consider this reasonable, as similar or larger discrepancy in bulk modulus is common for existing empirical potentials.

After being tested reliable for the ground-state configurations around every single phase, the potential is then used to study the phase transition. The phase transformation from the NiTi austenite to other phases is closely related to the imaginary frequency of the B2 phase phonon spectrum [50]. Here we compare the zero-temperature phonon dispersion of the austenite derived from the NNIP and DFT, as shown in Fig. 1. Specifically, the previous 2NN-MEAM potential [33] underestimates the imaginary frequency at M point by 1.5 THz, and also does not capture the imaginary frequency along Γ -R branch, which is another instability mode that

Table 1

Benchmark of the physical properties of equiatomic NiTi at 0 K calculated from the NNIP compared with the DFT results and previous 2NN MEAM potential. The quantities include: the lattice parameters a , b , c (Å), β (monoclinic angle, in degree), cohesive energy E (meV), bulk modulus B (GPa), and stiffness tensor C_{ij} (GPa).

Structure	Property	DFT	EAM/2NN-MEAM	NNIP (this work)
B2 ($Pm\bar{3}m$)	a	3.01 ^{a,d,e,f}	3.00 ^a , 3.02 ^{b,c}	2.99
	B	157.1 - 160 ^{a,f}	133.2 ^a , 295.7 ^b , 130 ^c	172.7
	C_{11}	183 ^g	146 ^c	183.7
	C_{12}	146, 153 ^g	122 ^c	167
	C_{44}	46 ^g	35 ^c	42.5
B19' ($P2_1/m$)	a	2.92 - 2.94 ^{a,d,e,f}	2.88 ^a , 2.87 ^b , 2.70 ^c	2.89
	b	4.03 - 4.05 ^{a,d,e,f}	4.13 ^a , 4.19 ^b , 4.39 ^c	4.03
	c	4.69 - 4.80 ^{a,d,e,f}	4.66 ^a , 4.62 ^b , 4.61 ^c	4.72
	β	100.0 - 102.4 ^{a,e,f}	99.4 ^a , 97.3 ^b	101.03
	$E_{B2} - E$	41.5 - 43.5 ^{a,d,e,f}	34.1 ^a , 32.9 ^b , 29 ^c	38.5
B19 ($P2_1/m$)	B	147 - 159 ^{a,f}	134 ^a , 141 ^c	164.2
	a	2.66 - 2.80 ^{a,d,e}	2.81 ^a , 2.88 ^c	2.74
	b	4.12 - 4.22 ^{a,d,e}	4.28 ^a , 4.36 ^c	4.25
	c	4.60 - 4.63 ^{a,d,e}	4.50 ^{a,c}	4.58
	$E_{B2} - E$	26.5 - 30 ^{a,d,e}	10.6 ^a , 15 ^c	25.2
B33 ($Cmcm$)	B	158.9 ^a	133.7 ^a	167.5
	a	2.91 - 2.94 ^{a,d,e,f}	3.15 ^a	2.88
	b	4.00 - 4.02 ^{a,d,e,f}	3.76 ^a	4.01
	c	4.92 - 4.94 ^{a,d,e,f}	4.98 ^a	4.84
	β	106.6 - 107.3 ^{a,d,e,f}	108.4 ^a	107.08
R ($Cmcm$)	$E_{B2} - E$	42 - 50 ^{a,d,e,f}	39.7 ^a	40.1
	B	149 - 157.8 ^{a,f}	127.5 ^a	164.1
	a	7.25	-	7.22
	c	5.40	-	5.37
	$E_{B2} - E$	17.8	-	16.6
	B	152		172.2

^a Ref. [33].

^b Ref. [41].

^c Ref. [34].

^d Ref. [7].

^e Ref. [42].

^f Ref. [43].

^g Ref. [44].

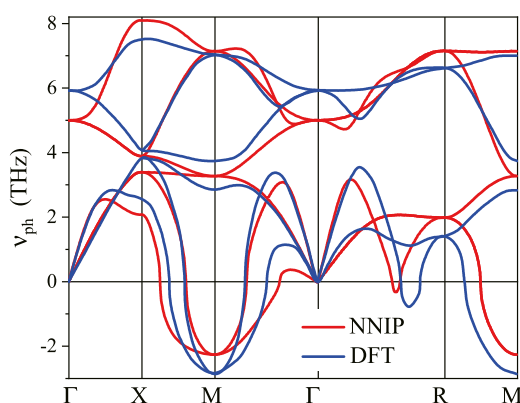


Fig. 1. Phonon dispersion of the B2 austenite at zero temperature. The red line is derived from the NNIP with $8 \times 8 \times 8$ supercell, and the DFT phonon dispersion is reproduced from Ref. [45]. (For interpretation of the references to colour in this figure legend, the reader is referred to the web version of this article.)

differs from the long-wavelength instability at Γ . The NNIP reproduces the qualitative features of the DFT phonon dispersion and shows smaller numerical discrepancy. The consistence examine that the NNIP can properly reproduce the *ab initio* atomic vibrations.

The temperature-induced phase transformation behavior is characterized by the finite-temperature free-energy curve on the martensitic transformation pathway shown in Fig. 2a. With increasing temperature, the free energy of the B19' phase is lifted relative to the B2 phase, deriving the experimentally observed temperature-induced martensitic transformation. The free energy

difference of B2 and B19' phase shows a good linear relationship with temperature from 300 to 450 K (Fig. 2b), crossing the zero point at 352 K, which falls in the range of representative transformation temperatures of 328–362 K in experiment [1]. Similar temperature-dependent free energy curves are also shown in the AIMD calculation [49] with consistent trend with the free energy curves in our simulation. In comparison, Ref. [49] shows a higher phase transformation temperature of 500 K. Although the origin of the difference can be complicated, our results show better consistency with experiments. We speculate that the difference can come from the supercell size (144-atom supercell in Ref. [49] and 864-atom supercell in our work) and phase transformation pathway (linear pathway in Ref. [49] and nudged elastic band pathway in our work). Also, evaluating (4) using classical MD ignores the quantum dynamics effects of Ni and Ti atoms. Although the origin of the difference could be complicated, our simulation scheme more effectively reproduces the experimental phase transformation behavior

The temperature- and stress-induced martensitic transformation can also be observed through direct MD simulation. In a periodic supercell MD calculation, the B2-B19' phase transformation spontaneously happens at 340 K during cooling and the inverse phase transformation happens at 600 K during the heating process (Fig. 3a). On the other hand, the B2-B19' phase transformation happens when a tensile stress is applied to the bulk crystal (Fig. 3b). The stress-strain curve shows evident superelastic behavior. Here we emphasize that the transition temperature and critical stress in the direct MD simulations are not directly comparable with experiment due to the spatial-scale and temporal-scale discrepancies with actual experiments [51]. As the martensitic transformation is a process of nucleation and growth, both μm -large size and ms-

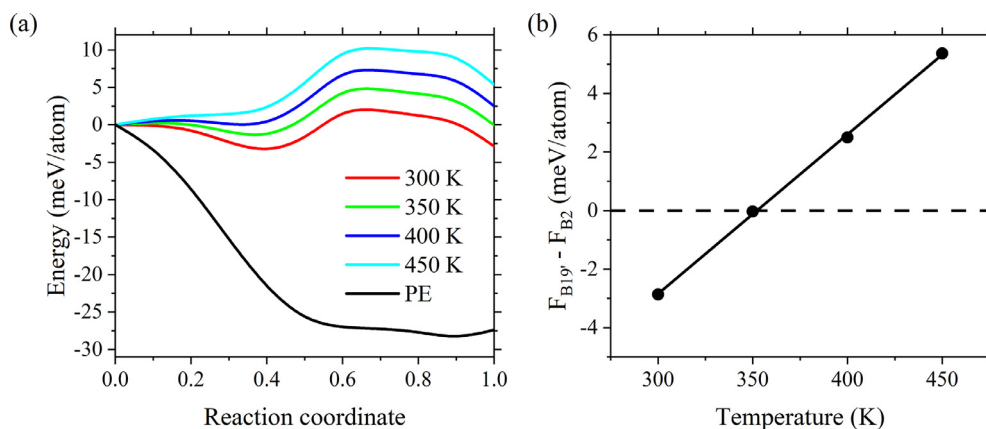


Fig. 2. Temperature-dependent phase stability of NiTi. (a) Helmholtz Free energy profile from the B2 phase (where reaction coordinate equals zero) to B19' phase (where reaction coordinate equals one) with different temperature. The free energy of the B2 phase is set as the zero point. (b) The temperature dependent free energy difference between the B19' and B2 phases.

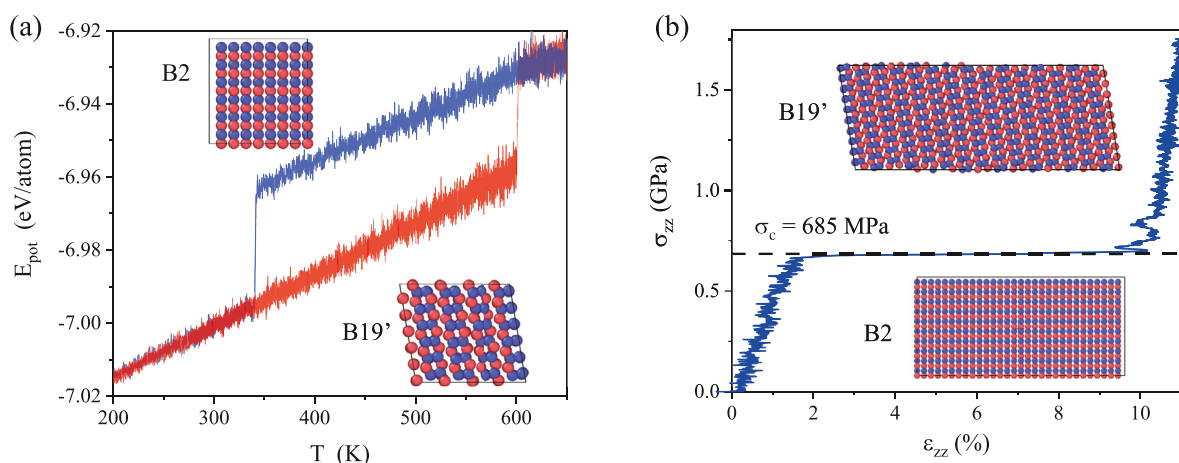


Fig. 3. (a) MD simulation of the potential energy *vs* temperature curve in the temperature-induced martensitic transformation. The blue line shows the cooling process while the red line shows the heating process. The cooling/heating rate is 2 K/ps, and the simulation box is a $6 \times 4 \times 4$ supercell of the B19' unit cell. (b) Stress-strain curve of the bulk NiTi during superelastic tensile deformation. The simulation box is a $10 \times 7 \times 15$ supercell of the B19' unit cell, and the loading rate is 13.3 MPa/ps perpendicular to the *ab*-plane of the B19' unit cell. Periodic boundary condition is applied to both (a) and (b). (For interpretation of the references to colour in this figure legend, the reader is referred to the web version of this article.)

long (or even longer) time are involved, which cannot be realized in direct simulation. In comparison, the thermodynamic integral of free energy in Fig. 2 gives a better prediction to experimental transition point.

Besides temperature, the martensitic transformation is also coupled with deformation twinning, which is proposed as a way to control elastic and plastic strain release [12–15]. A recent symmetry-based crystallography theory has predicted that the martensitic transformation could appear in the extended core structure of deformation twin boundary [9,52,53]. Using the NNIP direct simulation, we verified the prediction that the coupling between martensitic transformation and deformation twinning also exists in NiTi. The most commonly observed Σ_9 deformation twin boundary in the NiTi austenite is constructed, as shown in Fig. 4a. The MD simulation derives the formation of B19' phases that appear around the twin boundary at 400 K (above the martensitic transformation temperature), as shown in Fig. 4. The deformation twin extends to a nested twin boundary from B2 to B19' to twinned B19' to twinned B2 with a characteristic core width of about 2.5 nm, similar to the core width in the Ti-alloy experiment [16]. The twinning-induced NiTi B19' phase is well consistent with a recent transmission electron microscopy (TEM) study [12], as shown in Fig. 4d. Small B19' phase regions are identified be-

tween the B2 and B2_T region from both the real-space image and its Fast Fourier transform. Our MD simulation further shows that the core width of the twin boundary is continuously controlled by the temperature and external stress. Larger volume of the B19' phase will form at lower temperature or under shear stress. Compared to the sharp temperature-induced martensitic transformation, the twinning-induced martensitic transformation is controlled continuously by the intensive quantities, leading to low-hysteresis martensitic transformation curve. Therefore, this intrinsic coupling between the mechanical twinning and martensitic transformation during plastic deformation provides a mechanism for realizing low hysteresis, high strength superelasticity [14,54].

The superelasticity of NiTi nanowire is simulated directly by MD. First, a 3×3 nm-cross section NiTi nanowire is constructed and relaxed to equilibrium at 400 K (Fig. 5). Initially, the nanowire is in the B2 phase. Then, a tensile strain ϵ is applied to the NiTi nanowire. At $\epsilon = 10\%$, the martensite B19' phase appears in the nanowire (the B19' unit cell's *ab* plane is perpendicular to the nanowire orientation), accommodating part of the tensile strain. When ϵ approaches 18%, the maximal recoverable tensile strain according to our simulation, the nanowire completely transforms to the B19' phase. The martensitic transformation accompanies a shape change because of the shearing deformation in untwinned

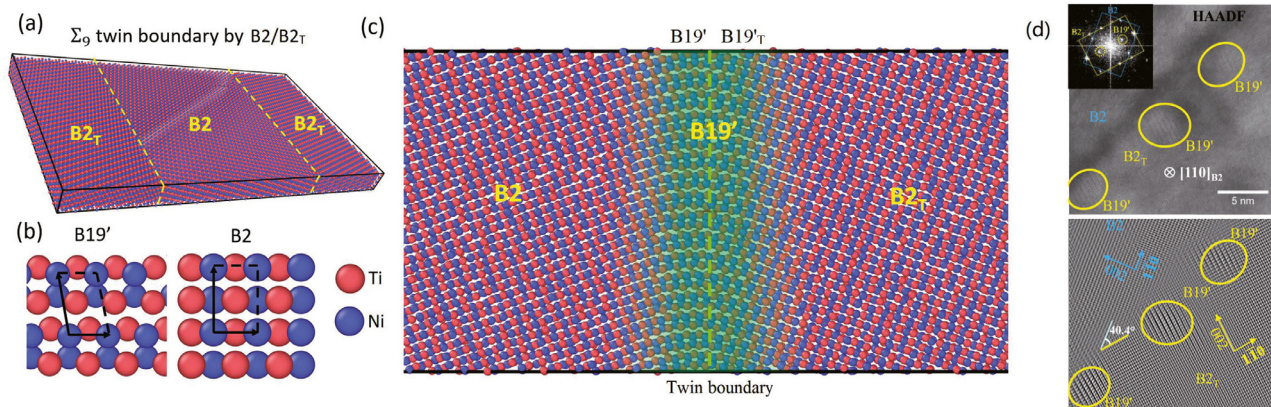


Fig. 4. Extended core structure of twin boundary in NiTi from the deep MD simulation. (a) Atomic structure of the Σ_9 ($\{114\}$ B2) lamellae deformation twin boundary (perfectly arranged), which is used as the initial state of the MD simulation. The structure contains 11,244 atoms with periodic boundary condition. (b) Atomic configuration of B2 and B19' viewed from (110) direction. (c) Atomic structure after 100 ps (20,000 iterations) of MD steps at 400 K viewed from (110) direction. (d) TEM analysis of the extend core structure of the NiTi Σ_9 twin boundary from Ref. [12].

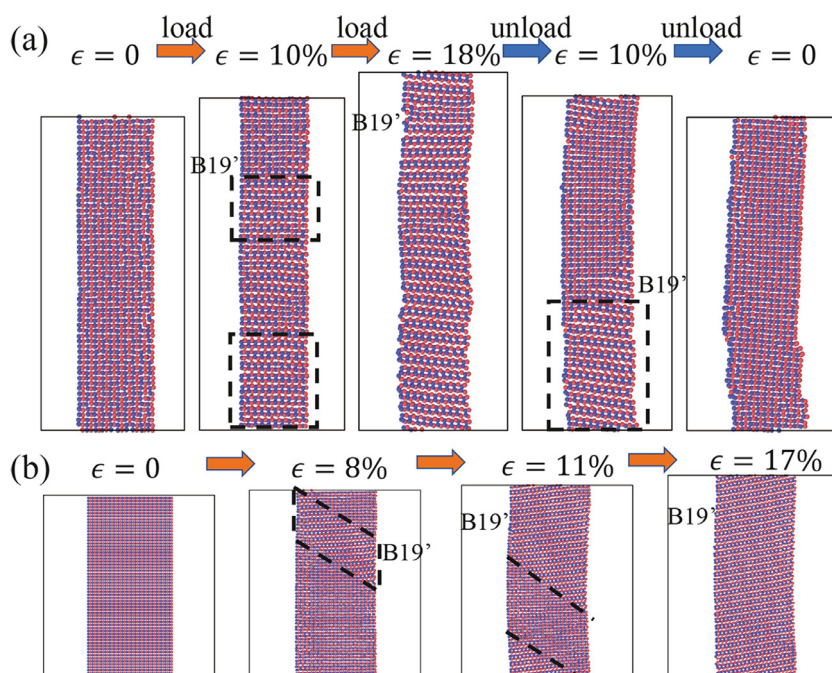


Fig. 5. Direct simulation of superelasticity in NiTi nanowires. (a) $3 \times 3 \times 12$ nm and (b) $6 \times 6 \times 12$ nm nanowires oriented to (B2 unit cell's) [110] direction are simulated with periodic boundary condition in the [110] direction. From left to right in (a), the figure shows the nanowire loaded to $\epsilon = 10\%$ and 18% , respectively, unloaded to $\epsilon = 10\%$, and finally fully unloaded. The loading rate in the MD simulation is $0.6\%/ps$. In (b), the nanowire is loaded to 17% with a loading rate of $0.2\%/ps$.

martensite. When we gradually unload the tensile strain in the nanowire, the B19' phase gradually transforms back to the B2 phase. The B2 phase is partially recovered at $\epsilon = 10\%$ and fully recovered when the external strain is further reduced. When the tensile stress is fully unloaded, the tensile deformation fully recovers (the residue tensile strain $\epsilon \simeq 0.1\%$ is within the fluctuation of the MD simulation), with a few horizontal slip traces left. Therefore, we predict that the NiTi nanowire exhibits superelastic behavior with a high recoverable strain of 18% . Similarly, high superelastic strain of 17% is observed in a nanowire with a larger cross section ($6nm \times 6nm$) (Fig. 5b), confirming that the superelasticity.

Different from the bulk superelasticity, the superelasticity of a nanowire is highly relevant to the surface effect [54]. As the (110) and (001) surface energy of the B2 phase is lower than that of the B19' counterparts, the surface energy effect impedes the martensitic transformation. Consequently, the critical stress of martensitic transformation under a given temperature is elevated by the

surface effect, leading to a higher strains in the nanowire when the transformation begins and completes, which contributes to the high overall superelastic strain. This observation is confirmed by comparing two nanowires with different cross section areas in Fig. 5. As the surface effect in the thin nanowire in Fig. 5a is more significant, its phase transformation initiates at $\epsilon_i = 9.3\%$ and ends at $\epsilon_f = 18.0\%$, larger than those observed for the thick nanowire (Fig. 5b) counterparts ($\epsilon_i = 7.7\%$ and $\epsilon_f = 16.3\%$). For increasing nanowire size, it is expected that the critical strain of the phase transformation will decrease, leading to a decreasing superelastic strain that approaches the bulk limit for high nanowire cross section

The simulation of superelasticity in nano-sized NiTi has also been implemented through empirical potentials [55,56]. However, as none of these potentials include surface or slab configurations in their fitting process, they can show unphysical results at the surface. As 2000 surface configurations are included in our training

and testing database, the NNIP can well reproduce the DFT surface energy. Therefore, this NNIP should provide a more reliable description of the surface effects that are essential in nano-object simulations.

Finally, we raise caution on using this NNIP for off-equiatom configurations. As all the training configuration is nearly equiatom, the NNIP is expected to give increasing extrapolation error for the increasing composition difference. Despite this, the NNIP gives reasonable results for composition within the NiTi phase region (without precipitates of Ti₂Ni and TiNi₃) according to our tests, which covers the composition range with the shape memory behavior [1]. To accurately simulate other alloy compositions like Ti₂Ni and TiNi₃, the NNIP needs reinforcement with larger training data set. Further training can derive a general NNIP that reproduces the full phase diagram for Ni-Ti binary alloy, and even chemically complex systems[57,58], which is left to future work.

4. Conclusion

In this work, we developed an NNIP for near-equiatom Ni-Ti with state-of-the-art accuracy. The performance of the NNIP is tested for both zero-temperature properties and temperature-induced phase transformation with good consistency with the DFT and experiments. Using the NNIP, the recently observed phase transformation caused by deformation twinning is successfully simulated for the first time. Benefiting from the reliable description of the surface structure, the superelasticity of NiTi nanowire is directly simulated. Our NiTi NNIP is publicly available through the interatomic potential repository (URL: <https://www.ctcms.nist.gov/potentials> Website doi:10.18434/m37), which interfaces with commonly used packages LAMMPS, ASE, and i-PI through DeepMD-kit. Our work provides a high-accuracy method to simulate the microstructure, SME, and superelasticity of NiTi, which will potentially contribute to the computational-guided structural engineering of SMA.

Declaration of Competing Interest

The authors declare that they have no known competing financial interests or personal relationships that could have appeared to influence the work reported in this paper.

Acknowledgments

We thank Longsheng Feng for insightful discussions. This work was supported by NSF DMR-1923976, NSF DMR-1923929 and NSF CMMI-1922206. The calculations in this work were performed in part on the Texas Advanced Computing Center (TACC) and the MIT engaging cluster.

References

- [1] D.C. Lagoudas, *Shape Memory Alloys: Modeling and Engineering Applications*, Springer, 2008.
- [2] H. Gu, L. Bumke, C. Chluba, E. Quandt, R.D. James, Phase engineering and supercompatibility of shape memory alloys, *Mater. Today* 21 (3) (2018) 265–277.
- [3] K. Otsuka, C.M. Wayman, *Shape Memory Materials*, Cambridge university press, 1999.
- [4] K. Otsuka, X. Ren, Physical metallurgy of ti–ni-based shape memory alloys, *Prog. Mater. Sci.* 50 (5) (2005) 511–678.
- [5] C. Jacson, 55-nitinol-the alloy with a memory: its physical metallurgy, properties and applications, NASA-SP-5110 15(1972).
- [6] Shape memory material technology insight report. [http://www.pateninsightpro.com/techreports/0315/tech insight report - shape memory materials.pdf](http://www.pateninsightpro.com/techreports/0315/tech%20insight%20report%20-%20shape%20memory%20materials.pdf) (accessed august 3, 2017), Patent iNSIGHT Pro-Gridlogics Technologies Pvt. Ltd. (2015).
- [7] X. Huang, G.J. Ackland, K.M. Rabe, Crystal structures and shape-memory behaviour of NiTi, *Nat Mater* 2 (5) (2003) 307–311.
- [8] J. Zhu, D. Wang, Y. Gao, T.-Y. Zhang, Y. Wang, Linear-superelastic metals by controlled strain release via nanoscale concentration-gradient engineering, *Mater. Today* 33 (2020) 17–23.
- [9] Y. Gao, Symmetry and pathway analyses of the twinning modes in Ni-Ti shape memory alloys, *Materialia* 6 (2019) 100320.
- [10] J. Zhu, Y. Gao, D. Wang, J. Li, T.-Y. Zhang, Y. Wang, Making metals linear super-elastic with ultralow modulus and nearly zero hysteresis, *Mater. Horiz.* 6 (3) (2019) 515–523.
- [11] J. Zhu, Y. Gao, D. Wang, T.-Y. Zhang, Y. Wang, Taming martensitic transformation via concentration modulation at nanoscale, *Acta Mater.* 130 (2017) 196–207.
- [12] Q. Liang, S. Zhao, D. Wang, J. Zhang, S. Li, Y. Wang, Y. Zheng, X. Ren, M. Mills, Y. Wang, Strain states and unique properties in cold-rolled TiNi shape memory alloys, submitted to *Acta Mater.* (May 2021, to be published).
- [13] Q. Liang, D. Wang, J. Zhang, Y. Ji, X. Ding, Y. Wang, X. Ren, Y. Wang, Novel b19' strain glass with large recoverable strain, *Phys. Rev. Mater.* 1 (3) (2017) 033608.
- [14] Y. Gao, Y. Zheng, H. Fraser, Y. Wang, Intrinsic coupling between twinning plasticity and transformation plasticity in metastable β ti-alloys: a symmetry and pathway analysis, *Acta Mater.* 196 (2020) 488–504.
- [15] S. Antonov, Z. Kloenne, Y. Gao, D. Wang, Q. Feng, Y. Wang, H.L. Fraser, Y. Zheng, Novel deformation twinning system in a cold rolled high-strength metastable- β ti-5al-5v-5mo-3cr-0.5 fe alloy, *Materialia* 9 (2020) 100614.
- [16] Q. Liang, Z. Kloenne, Y. Zheng, D. Wang, S. Antonov, Y. Gao, Y. Hao, R. Yang, Y. Wang, H.L. Fraser, The role of nano-scaled structural non-uniformities on deformation twinning and stress-induced transformation in a cold rolled multifunctional β -titanium alloy, *Scr. Mater.* 177 (2020) 181–185.
- [17] Q. Liang, D. Wang, Y. Zheng, S. Zhao, Y. Gao, Y. Hao, R. Yang, D. Banerjee, H.L. Fraser, Y. Wang, Shuffle-nanodomain regulated strain glass transition in ti-24nb-4zr-8sn alloy, *Acta Mater.* 186 (2020) 415–424.
- [18] J. Zhu, H.-H. Wu, Y. Wu, H. Wang, T. Zhang, H. Xiao, Y. Wang, S.-Q. Shi, Influence of ni4ti3 precipitation on martensitic transformations in NiTi shape memory alloy: R phase transformation, *Acta Mater.* 207 (2021) 116665.
- [19] S. Gur, G.N. Frantzikonis, K. Muralidharan, Atomistic simulation of shape memory effect (SME) and superelasticity (se) in nano-porous NiTi shape memory alloy (SMA), *Comput. Mater. Sci.* 152 (2018) 28–37.
- [20] S. Liu, Y. Lin, L. Han, X. Wang, G. Zhao, G. Wang, Atomistic simulation of microstructure evolution of NiTi single crystals in bending deformation, *Comput. Mater. Sci.* 199 (2021) 110733.
- [21] A.S.K. Mohammed, H. Sehitoglu, Modeling the interface structure of type ii twin boundary in b19 NiTi from an atomistic and topological standpoint, *Acta Mater.* 183 (2020) 93–109.
- [22] B. Wang, G. Kang, W. Wu, K. Zhou, Q. Kan, C. Yu, Molecular dynamics simulations on nanocrystalline super-elastic NiTi shape memory alloy by addressing transformation ratchetting and its atomic mechanism, *Int. J. Plast.* 125 (2020) 374–394.
- [23] Y. Zhong, K. Gall, T. Zhu, Atomistic study of nanotwins in NiTi shape memory alloys, *J. Appl. Phys.* 110 (3) (2011) 033532.
- [24] D. Marx, J. Hutter, *Ab InitioMolecular Dynamics: Basic Theory and Advanced Methods*, Cambridge University Press, 2009.
- [25] D. Farkas, D. Roqueta, A. Vilette, K. Ternes, Atomistic simulations in ternary Ni - Ti - al alloys, *Modell. Simul. Mater. Sci. Eng.* 4 (4) (1996) 359–369, doi:10.1088/0965-0393/4/4/003.
- [26] M.S. Daw, M.I. Baskes, Embedded-atom method: derivation and application to impurities, surfaces, and other defects in metals, *Phys. Rev. B* 29 (12) (1984) 6443.
- [27] W. Lai, B. Liu, Lattice stability of some Ni-Ti alloy phases versus their chemical composition and disordering, *J. Phys.: Condens. Matter* 12 (5) (2000) L53.
- [28] M. Finnis, J. Sinclair, A simple empirical n-body potential for transition metals, *Philos. Mag.* A 50 (1) (1984) 45–55.
- [29] K.-i. Saitoh, K. Kubota, T. Sato, Atomic-level structural change in Ni-Ti alloys under martensite and amorphous transformations, *Tech. Mech. Eur. J. Eng. Mech.* 30 (1–3) (2010) 269–279.
- [30] H. Ishida, Y. Hiwatari, Md simulation of martensitic transformations in tini alloys with meam, *Mol. Simul.* 33 (4–5) (2007) 459–461.
- [31] M.I. Baskes, Modified embedded-atom potentials for cubic materials and impurities, *Phys. Rev. B* 46 (5) (1992) 2727.
- [32] P. Srinivasan, A.I. Duff, T.A. Mellan, M.H. Sluiter, L. Nicola, A. Simone, The effectiveness of reference-free modified embedded atom method potentials demonstrated for NiTi and nbmotaw, *Modell. Simul. Mater. Sci. Eng.* 27 (6) (2019) 065013.
- [33] W.-S. Ko, B. Grabowski, J. Neugebauer, Development and application of a Ni-Ti interatomic potential with high predictive accuracy of the martensitic phase transition, *Phys. Rev. B* 92 (13) (2015) 134107.
- [34] G. Ren, H. Sehitoglu, Interatomic potential for the NiTi alloy and its application, *Comput. Mater. Sci.* 123 (2016) 19–25.
- [35] L. Zhang, J. Han, H. Wang, R. Car, E. Weinan, Deep potential molecular dynamics: a scalable model with the accuracy of quantum mechanics, *Phys. Rev. Lett.* 120 (14) (2018) 143001.
- [36] H. Wang, L. Zhang, J. Han, E. Weinan, Deepmd-kit: a deep learning package for many-body potential energy representation and molecular dynamics, *Comput. Phys. Commun.* 228 (2018) 178–184.
- [37] Y. Zhang, H. Wang, W. Chen, J. Zeng, L. Zhang, H. Wang, E. Weinan, Dp-gen: a concurrent learning platform for the generation of reliable deep learning based potential energy models, *Comput. Phys. Commun.* 253 (2020) 107206.

- [38] G. Kresse, J. Furthmüller, Efficient iterative schemes for *ab initio* total-energy calculations using a plane-wave basis set, *Phys. Rev. B* 54 (16) (1996) 11169.
- [39] G. Kresse, D. Joubert, From ultrasoft pseudopotentials to the projector augmented-wave method, *Phys. Rev. B* 59 (3) (1999) 1758.
- [40] J.P. Perdew, K. Burke, M. Ernzerhof, Generalized gradient approximation made simple, *Phys. Rev. Lett.* 77 (18) (1996) 3865.
- [41] S. Kavousi, B.R. Novak, M.I. Baskes, M.A. Zaeem, D. Moldovan, Modified embedded-atom method potential for high-temperature crystal-melt properties of ti-ni alloys and its application to phase field simulation of solidification, *Modell. Simul. Mater. Sci. Eng.* 28 (1) (2019) 015006.
- [42] K.G. Vishnu, A. Strachan, Phase stability and transformations in NiTi from density functional theory calculations, *Acta Mater.* 58 (3) (2010) 745–752.
- [43] D. Holec, M. Friák, A. Dlouhý, J. Neugebauer, *Ab initio* study of pressure stabilized NiTi allotropes: pressure-induced transformations and hysteresis loops, *Phys. Rev. B* 84 (22) (2011) 224119.
- [44] N. Hatcher, O.Y. Kontsevoi, A.J. Freeman, Role of elastic and shear stabilities in the martensitic transformation path of NiTi, *Phys. Rev. B* 80 (14) (2009) 144203.
- [45] K. Parlinski, M. Parlinska-Wojtan, Lattice dynamics of NiTi austenite, martensite, and R phase, *Phys. Rev. B* 66 (6) (2002) 064307.
- [46] A.P. Thompson, H.M. Aktulga, R. Berger, D.S. Bolintineanu, W.M. Brown, P.S. Crozier, P.J. in't Veld, A. Kohlmeyer, S.G. Moore, T.D. Nguyen, et al., LAMMPS—a flexible simulation tool for particle-based materials modeling at the atomic, meso, and continuum scales, *Comput. Phys. Commun.* 271 (2022) 108171.
- [47] D.J. Evans, B.L. Holian, The nose–hoover thermostat, *J. Chem. Phys.* 83 (8) (1985) 4069–4074.
- [48] C. Jarzynski, Nonequilibrium equality for free energy differences, *Phys. Rev. Lett.* 78 (14) (1997) 2690.
- [49] J.B. Haskins, A.E. Thompson, J.W. Lawson, *Ab initio* simulations of phase stability and martensitic transitions in NiTi, *Phys. Rev. B* 94 (21) (2016) 214110.
- [50] X. Huang, C. Bungaro, V. Godlevsky, K.M. Rabe, Lattice instabilities of cubic NiTi from first principles, *Phys. Rev. B* 65 (1) (2001) 014108.
- [51] J. Li, The mechanics and physics of defect nucleation, *MRS Bull.* 32 (2007) 151–159.
- [52] Y. Gao, S.A. Dregia, Y. Wang, A universal symmetry criterion for the design of high performance ferroic materials, *Acta Mater.* 127 (2017) 438–449.
- [53] Y. Gao, L. Casalena, M. Bowers, R. Noebe, M. Mills, Y. Wang, An origin of functional fatigue of shape memory alloys, *Acta Mater.* 126 (2017) 389–400.
- [54] Q. Liang, Y. Zheng, D. Wang, Y. Hao, R. Yang, Y. Wang, H.L. Fraser, Nano-scale structural non-uniformities in gum like ti-24nb-4zr-8sn metastable β -ti alloy, *Scr. Mater.* 158 (2019) 95–99.
- [55] Y. Zhong, K. Gall, T. Zhu, Atomistic characterization of pseudoelasticity and shape memory in NiTi nanopillars, *Acta Mater.* 60 (18) (2012) 6301–6311.
- [56] D. Mutter, P. Nielaba, Simulation of the shape memory effect in a NiTi nano model system, *J. Alloy. Compd.* 577 (2013) S83–S87.
- [57] S. Takamoto, S. Izumi, J. Li, Teanet: universal neural network interatomic potential inspired by iterative electronic relaxations, *Comput. Mater. Sci.* 207 (2022) 111280.
- [58] S. Takamoto, C. Shinagawa, D. Motoki, K. Nakago, W. Li, I. Kurata, T. Watanabe, Y. Yayama, H. Iriguchi, Y. Asano, T. Onodera, T. Ishii, T. Kudo, H. Ono, R. Sawada, R. Ishitani, M. Ong, T. Yamaguchi, T. Kataoka, A. Hayashi, N. Charoenphakdee, T. Ibuka, Towards universal neural network potential for material discovery applicable to arbitrary combination of 45 elements, *Nat. Commun.* 13 (2022) 2991.